The Journal of Chemical Physics

Correlated spectral fluctuations quantified by line shape analysis of fifth-order two-dimensional electronic spectra

Cite as: J. Chem. Phys. **156**, 084114 (2022); https://doi.org/10.1063/5.0081053
Submitted: 06 December 2021 • Accepted: 01 February 2022 • Accepted Manuscript Online: 02 February 2022 • Published Online: 24 February 2022

Constantin Heshmatpour, Jürgen Hauer and František Šanda

The Journal of Chemical Physics ARTICLE scitation.org/journal/jcp

Correlated spectral fluctuations quantified by line shape analysis of fifth-order two-dimensional electronic spectra

Cite as: J. Chem. Phys. 156, 084114 (2022); doi: 10.1063/5.0081053
Submitted: 6 December 2021 • Accepted: 1 February 2022 •
Published Online: 24 February 2022

Constantin Heshmatpour,[1,2] Jürgen Hauer,[2] and František Šanda[1,a)]

AFFILIATIONS

[1] Institute of Physics, Faculty of Mathematics and Physics, Charles University, Ke Karlovu 5, Prague 121 16, Czech Republic
[2] Professur für Dynamische Spektroskopien, Fakultät für Chemie, Technische Universität München, Lichtenbergstr. 4, D-85748 Garching b. München, Germany

Note: This paper is part of the JCP Special Topic on Photosynthetic Light-Harvesting and Energy Conversion.
[a)] **Author to whom correspondence should be addressed:** sanda@karlov.mff.cuni.cz

ABSTRACT

Correlated spectral fluctuations were suggested to coordinate excitation transport inside natural light harvesting complexes. We demonstrate the capacities of 2D line shapes from fifth-order coherent electronic signals (R^5-2D) to report on such fluctuations in molecular aggregates and present a stochastic approach to fluctuations in correlated site and bi-exciton binding energies in the optical dynamics of Frenkel excitons. The model is applied to R^5-2D line shapes of a homodimer, and we show that the peak tilt dynamics are a measure for site energy disorder, inter-site correlation, and the strength of bi-exciton binding energy fluctuations.

I. INTRODUCTION

The remarkably high energy transfer efficiencies found in photosynthesis rests on pigment–protein complexes. In light harvesting antennas, the protein arranges strongly absorbing chromophores in close proximity with inter-pigment distances on the order of 10 Å. Upon photoexcitation, their specific steric arrangement leads to the formation of delocalized excitons. Their dynamics determine the observed high energy transfer efficiencies beyond standard transport theories.[1] The intricate role played by the pigment–protein interactions is at the heart of a long-lasting scientific debate. The theoretical approaches to this fascinating problem have been reviewed elsewhere[2] and can be categorized into theories focusing on the role of high-frequency underdamped vibrations facilitating transport via vibronic resonances[3,4] and theories emphasizing the role of the protein in coordinating low-frequency vibrational modulations of pigments. Such correlations between site frequencies[5] were suggested to prolong the excitonic coherence lifetime, and the effect of such protected coherent states on transfer efficiency is a topic of the current debate.[6] The experimental evidence for such correlated fluctuations is mainly derived from two-dimensional electronic spectroscopy or R^3-2D and relies heavily on the analysis of relatively weak beating features.[7] In this work, we show that fifth order or R^5-2D spectroscopy gives more direct access to site correlation effects in excitonic systems as well as spectral fluctuations of bi-exciton binding energies. The inclusion of the latter has been shown to be instrumental to obtain an agreement between simulated and measured non-linear line shapes of photosynthetic reaction centers at low temperatures.[8]

In general terms, R^5-2D electronic spectroscopy is a three pulse experiment measured along $\vec{K}_{R,NR} = \mp 2\vec{K}_1 \pm 2\vec{K}_2 + \vec{K}_3$ phase matching directions. Such signals were shown to specifically address the relaxation pathways of bi-excitons,[9,10] with emphasis on exciton–exciton annihilation[11] (EEA); this process is not directly accessible in experiments of lower orders. The alluring feature of R^5-2D is that—in homoaggregates with aligned transition dipoles—all inter-band transport contributions cancel by integrating the R^5-2D signal over excitation frequency Ω_1 and emission frequency Ω_3 for every waiting time t_2.[12] The integrated signal of aligned homoaggregates, thus, allows us to exclusively track and pinpoint annihilation dynamics. For non-aligned structures, annihilation and transport contributions are intertwined in

the integrated signal,[12] but the anisotropy in the integrated signal reports on the geometry of the aggregate.[13] However, annihilation dynamics in non-aligned aggregates can still be obtained from the R^5-2D signal by following the temporal evolution of specific peaks.[14]

First, R^5-2D experiments studied the diffusion limited annihilation processes in various large molecular J-aggregates to extract the picosecond exciton diffusion timescale controlling the rate of annihilation.[10,15] We have in contrast recently directly measured the ultrafast annihilation timescale of 30 fs inside a squaraine trimer.[14] The annihilation rate was extracted by following the peak volume dynamics of a single peak employing a Markovian master equation model.[12] We omitted a detailed line shape analysis as the employed model provides purely homogeneous line shapes despite the fact that the data showed interesting features such as a clearly recognizable nodal line tilt and signs of dynamic disorder, i.e., line shape dynamics. Such processes represent slow fluctuations of transition energies as studied extensively in 2D infrared spectroscopy (2D-IR)[16,17] and third order 2D electronic spectroscopy (R^3-2D). The said line shape changes—quantified by the center line (CL) slope, eccentricity, or nodal line of 2D line shapes—have been instrumental to evaluate environmental characteristics such as the system's frequency correlation function.[18]

In the present paper, we develop an accessible theoretical approach to address signatures of dynamic disorder in R^5-2D line shapes of small molecular aggregates and extend the developed master equation of Ref. 12—limited to fast environmental fluctuations—by slow spectral fluctuations responsible for line shape dynamics.[19] The latter are approximated by a classical stochastic Gaussian modulation[20,21] of site and bi-exciton binding energies. The developed model is employed to analyze R^5-2D line shape dynamics of molecular homodimers with H-type coupling (H-homodimer). We find that the inclusion of dynamic disorder introduces a tilt in the line shapes at $t_2 = 0$ fs, which we demonstrate to encode the sign and amount of correlations between on-site energies and additionally the fluctuation magnitude of the bi-exciton binding energy. We quantify and analyze the temporal evolution of the tilted line shapes by the means of center lines, introduced to extract frequency correlations from R^3-2D and 2D-IR spectra.[17,18]

II. MODEL

We consider a molecular aggregate consisting of N coupled two level molecules. The electronic level structure and transport dynamics within this system is described by the Frenkel exciton Hamiltonian[22]

$$\hat{H}(t) = \sum_{n=1}^{N} \hat{E}_n(t)\hat{B}_n^\dagger \hat{B}_n + \sum_{\substack{n,m=1 \\ n\neq m}}^{N} J_{nm}\hat{B}_n^\dagger \hat{B}_m + \sum_{\substack{n,m=1 \\ n\neq m}}^{N} \frac{\hat{\Delta}_{nm}(t)}{2}\hat{B}_n^\dagger \hat{B}_m^\dagger \hat{B}_n \hat{B}_m. \tag{1}$$

Site energies $\hat{E}_n(t)$ and bi-exciton binding energies $\hat{\Delta}_{nm}(t)$ are subject of stochastic bath induced modulations. The excitonic coupling J_{nm} is assumed to be constant as its modulations are usually quite weak and have negligible influence on line shapes.[23] $\hat{B}_n^\dagger$ and $\hat{B}_n$ are, respectively, the operators associated with excitation and de-excitation of site n obeying the Pauli commutation relation,[24]

$$\left[\hat{B}_n, \hat{B}_m^\dagger\right] = \delta_{mn}\left(1 - 2\hat{B}_m^\dagger \hat{B}_n\right). \tag{2}$$

We further assume that the stochastic modulation of $\hat{H}(t)$ around mean values $\bar{E}_n$ ($\bar{\Delta}_{nm}$) of on-site (bi-exciton binding) energies can be decomposed into slow classical $E_n(t)$ ($\Delta_{nm}(t)$) and fast quantum $\hat{Q}_n$ ($\hat{Q}_{nm}$) components. The slow classical components are Gaussian[25] and are thus fully characterized by the correlation matrices

$$\begin{aligned}
\Sigma^{(1)}_{n,m}(t) &\equiv \left\langle \left(E_n(t) - \bar{E}_n\right)\left(E_m(0) - \bar{E}_m\right)\right\rangle, \\
\Sigma^{(2)}_{nm,kl}(t) &\equiv \left\langle \left(\Delta_{nm}(t) - \bar{\Delta}_{nm}\right)\left(\Delta_{kl}(0) - \bar{\Delta}_{kl}\right)\right\rangle, \\
\Sigma^{(2-1)}_{nm,k}(t) &\equiv \left\langle \left(\Delta_{nm}(t) - \bar{\Delta}_{nm}\right)\left(E_k(0) - \bar{E}_k\right)\right\rangle.
\end{aligned} \tag{3}$$

For simulations, it is feasible to decompose the Gaussian processes $E_n(t)$ and $\Delta_{nm}(t)$,

$$E_n(t) = \bar{E}_n + \sum_{m=1}^{N_q} D_{nm} q_m(t), \tag{4}$$

$$\Delta_{nm}(t) = \bar{\Delta}_{nm} + \sum_{k=1}^{N_q} \tilde{D}_{nm,k} q_k(t), \tag{5}$$

into linear combinations of N_q independent Ornstein–Uhlenbeck[20] (OU) processes $q_n(t)$, characterized by the exponentially decaying correlation function

$$C_n^{(q)}(t) = \langle q_n(t) q_n(0)\rangle = \sigma_n^2 e^{-t/\tau_n}, \tag{6}$$

with timescale τ_n and magnitude σ_n. Correlations among site and bi-exciton binding energies or between the two are then encoded in coefficients D_{nm} and $\tilde{D}_{nm,k}$ as inserting Eqs. (4) and (5) into Eq. (3) leads to

$$\begin{aligned}
\Sigma^{(1)}_{n,m}(t) &= \sum_{j=1}^{N_q} D_{nj} D_{mj} C_j^{(q)}(t), \\
\Sigma^{(2)}_{nm,kl}(t) &= \sum_{j=1}^{N_q} \tilde{D}_{nm,j} \tilde{D}_{kl,j} C_j^{(q)}(t), \\
\Sigma^{(2-1)}_{nm,k}(t) &= \sum_{j=1}^{N_q} \tilde{D}_{nm,j} D_{kj} C_j^{(q)}(t).
\end{aligned} \tag{7}$$

The above decomposition of the matrices Σ combines a separation of timescales τ_n with the decomposition into products of the type DD^T, which can be numerically obtained employing the Cholesky factorization algorithm.[26]

In the calculation scheme of the non-linear response functions, presented below, the two point joint probability

$$P(q_n(t), q_n(0), t) = \frac{1}{2\pi\sigma_n^2\sqrt{\left(1 - e^{-2t/\tau_n}\right)}} \times \exp\left(-\frac{q_n^2(t) + q_n^2(0) - 2q_n(t)q_n(0)e^{-\frac{t}{\tau_n}}}{2\sigma_n^2\left(1 - e^{-2t/\tau_n}\right)}\right) \tag{8}$$

of the OU process [Eq. (6)] will be of special importance.

The fast coordinates $\hat{Q}_n$ and $\hat{Q}_{nm}$ induce transport and decoherence and are considered quantum to ensure thermodynamic consistence.[27] We take advantage of the timescale separation between the slow and fast coordinates and include the effect of $\hat{Q}_n$ and $\hat{Q}_{nm}$ by a quantum master equation whose derivation is well documented in the literature[27] and shortly summarized in Appendix A. The resulting excitonic master equation

$$\frac{\partial}{\partial t}|\rho(t)\rangle\rangle = \check{\mathscr{R}}(\{q(t)\})|\rho(t)\rangle\rangle \tag{9}$$

with relaxation tensor

$$\check{\mathscr{R}}(\{q(t)\}) = \check{\mathscr{L}}(\{q(t)\}) + \check{\mathscr{D}}(\{q(t)\}) + \check{\mathscr{A}} \tag{10}$$

depends on the collection of slow coordinates $\{q(t)\} = (q_1(t), q_2(t), \ldots, q_n(t))$ and consists out of three parts: Liouvillian of the free evolution

$$\check{\mathscr{L}}(\{q(t)\})|\rho(t)\rangle\rangle = -i[H(t), \hat{\rho}(t)] \tag{11}$$

generated by the slow (classical) part of Hamiltonian (1), i.e., by substituting solely Eqs. (4) and (5) for site $\hat{E}$ and bi-exciton binding energies $\hat{\Delta}$ into Eq. (1). Dissipative dynamics $\check{\mathscr{D}}(\{q(t)\})$ generated by the fast component is calculated in the Redfield[28] limit and induces homogeneous line broadening and population relaxation. $\check{\mathscr{A}}$ describes EEA as unidirectional transfer between manifolds differing in one quantum of excitation with phenomenological rates k_i^A $(i = 1, \ldots, N-1)$. Our model thus omits a detailed microscopic description of EEA via an additional transient local state[29–31] and represents the minimal model retaining only the most essential structure of the manifolds and transport processes required for simulating peak shapes of R^5-2D signals. The detailed equations can be found in Appendix A.

To calculate the fifth-order response emitted into rephasing $(\vec{K}_R = -2\vec{K}_1 + 2\vec{K}_2 + \vec{K}_3)$ and non-rephasing $(\vec{K}_{NR} = 2\vec{K}_1 - 2\vec{K}_2 + \vec{K}_3)$ phase matching directions, we employ Kubo theory and the impulsive limit.[32,33] The interaction between the aggregate and the electric field $\mathscr{E}(t) = \sum_{j=1}^{3}\mathscr{E}_j\delta(t-\tau_j)$ is described semi-classically,

$$\hat{H}_{int}(t) = -\hat{\mu}\mathscr{E}(t) + c.c, \tag{12}$$

where $\hat{\mu} = \sum_{n=1}^{N} d_n \hat{B}_n^\dagger$ is the total dipole operator and d_n is the transition dipole moment of molecule n. To include the stochastic dynamics of Eqs. (3)–(11) into the model, we adapt the calculation strategy of Ref. 34: First, we calculate the non-linear response functions along non-rephasing and rephasing phase matching directions for a specific trajectory $\{\not{q}(t)\}$, and later, we average over all possible trajectories. We employ the Liouville space notation,[35,36] with inner product $\langle\langle A||B\rangle\rangle \equiv \mathrm{Tr}\,\hat{A}^\dagger\hat{B}$. The excitonic density matrix element before the first light–matter interaction, with the system in its ground state, reads as $|gg\rangle\rangle$. By using Green's function superoperator technique,[24] one obtains

$$\begin{aligned} S_{NR}^{(5)}(t_1,t_2,t_3;\{\not{q}(\tau)\}) = (i)^5\langle\langle\mu|\check{\mathscr{G}}(t_1+t_2,t_1+t_2+t_3;\{\not{q}(\tau)\})\check{\mu}^{(+)} \\ \times\check{\mathscr{G}}(t_1,t_1+t_2;\{\not{q}(\tau)\})\check{\mu}^{(-)}\check{\mu}^{(-)} \\ \times\check{\mathscr{G}}(0,t_1;\{\not{q}(\tau)\})\check{\mu}^{(+)}\check{\mu}^{(+)}|gg\rangle\rangle \end{aligned} \tag{13}$$

for the non-rephasing signal and

$$\begin{aligned} S_{R}^{(5)}(t_1,t_2,t_3;\{\not{q}(\tau)\}) = (i)^5\langle\langle\mu|\check{\mathscr{G}}(t_1+t_2,t_1+t_2+t_3;\{\not{q}(\tau)\})\check{\mu}^{(+)} \\ \times\check{\mathscr{G}}(t_1,t_1+t_2;\{\not{q}(\tau)\})\check{\mu}^{(+)}\check{\mu}^{(+)} \\ \times\check{\mathscr{G}}(0,t_1;\{\not{q}(\tau)\})\check{\mu}^{(-)}\check{\mu}^{(-)}|gg\rangle\rangle \end{aligned} \tag{14}$$

for the rephasing signal. The dipole superoperators $\check{\mu}^{(+)} \equiv \sum_{n=1}^{N} d_n(\check{B}_{nl}^\dagger - \check{B}_{nr}^\dagger)$ and $\check{\mu}^{(-)} \equiv \sum_{n=1}^{N} d_n(\check{B}_{nl} - \check{B}_{nr})$ are defined employing left $\check{B}_l|A\rangle\rangle \equiv \hat{B}\hat{A}$ and right $\check{B}_r|A\rangle\rangle \equiv \hat{A}\hat{B}$ multiplication superoperators. The response functions (13) and (14) and Green's function solution to the excitonic master equation (9),

$$\check{\mathscr{G}}(t_a,t_b;\{\not{q}(\tau)\}) = \exp_+\left\{\int_{t_a}^{t_b} d\tau\check{\mathscr{R}}(\{q(\tau)\})\right\}, \tag{15}$$

depend on the entire stochastic trajectories, what we emphasized by the $\{\not{q}(t)\}$ notation. To calculate the final response functions, we have to perform as the next step an average over the complete collection of stochastic paths. To facilitate the non-trivial averaging procedure, we again employ the slow character of coordinates $q(t)$ and assume that they are stable during the short coherence intervals t_1 and t_3. Green's function (15) then parametrically depends on the value of $q(t)$ at single time. The explicit dependence of the superoperator exponential on both the initial (t_a) and final (t_b) time then reduces to a function of the interval $t_b - t_a$. In particular, in the t_1 interval, we have

$$\check{\mathscr{G}}(0,t_1;\{\not{q}(\tau)\}) \approx \check{\mathscr{G}}(t_1;\{q(0)\}) = \exp\{\check{\mathscr{R}}(\{q(0)\})t_1\} \tag{16}$$

and in the t_3 interval, we have

$$\begin{aligned} \check{\mathscr{G}}(t_1+t_2,t_1+t_2+t_3;\{\not{q}(\tau)\}) &\approx \check{\mathscr{G}}(t_3;\{q(t_2)\}) \\ &= \exp\{\check{\mathscr{R}}(\{q(t_2)\})t_3\}. \end{aligned} \tag{17}$$

In population interval t_2, we allow for the changes in q coordinates, but the associated relaxation dynamics will only be re-parameterized in the middle of the interval.[37] Green's function thus propagates half of the t_2 interval with $\check{\mathscr{R}}$ taken at $q(0)$ and the remaining part with $q(t_2)$. These assumptions lead to the non-rephasing signal

$$\begin{aligned} &S_{NR}^{(5)}(t_1,t_2,t_3;\{\not{q}(\tau)\}) \\ &\approx (i)^5\langle\langle\mu|\check{\mathscr{G}}(t_3;\{q(t_2)\})\check{\mu}^{(+)}\check{\mathscr{G}}\left(\frac{t_2}{2};\{q(t_2)\}\right)\check{\mathscr{G}}\left(\frac{t_2}{2};\{q(0)\}\right) \\ &\quad\times\check{\mu}^{(-)}\check{\mu}^{(-)}\check{\mathscr{G}}(t_1;\{q(0)\})\check{\mu}^{(+)}\check{\mu}^{(+)}|gg\rangle\rangle \end{aligned} \tag{18}$$

and the rephasing signal

$$\begin{aligned} &S_{R}^{(5)}(t_1,t_2,t_3;\{\not{q}(\tau)\}) \\ &\approx (i)^5\langle\langle\mu|\check{\mathscr{G}}(t_3;\{q(t_2)\})\check{\mu}^{(+)}\check{\mathscr{G}}\left(\frac{t_2}{2};\{q(t_2)\}\right)\check{\mathscr{G}}\left(\frac{t_2}{2};\{q(0)\}\right) \\ &\quad\times\check{\mu}^{(+)}\check{\mu}^{(+)}\check{\mathscr{G}}(t_1;\{q(0)\})\check{\mu}^{(-)}\check{\mu}^{(-)}|gg\rangle\rangle \end{aligned} \tag{19}$$

Equations (18) and (19) now depend on q at time zero and a single t_2 value at a later time, and the final averaging $\langle\cdots\rangle$ of rephasing and non-rephasing signals of the fifth-order response over stochastic trajectories is then performed with the two time joint probabilities introduced in Eq. (8), resulting in

$$\begin{aligned} R^{(5)}_{R;NR}(t_1,t_2,t_3) &= \langle S^{(5)}_{R;NR}(t_1,t_2,t_3;\{q(\tau)\})\rangle \\ &\approx \prod_{n=1}^{N_q}\left(\int_{-\infty}^{\infty} dq_n(t_2)\int_{-\infty}^{\infty} dq_n(0)\right) \\ &\times S^{(5)}_{R;NR}(t_1,t_2,t_3;\{q(t_2)\},\{q(0)\}) \\ &\times \prod_{n=1}^{N_q} P(q_n(t_2),q_n(0),t_2). \end{aligned} \tag{20}$$

The purely absorptive line shapes of the R^5-2D signal

$$\tilde{R}_{2D}(\Omega_1,t_2,\Omega_3) \equiv \tilde{R}_R(\Omega_1,t_2,\Omega_3) + \tilde{R}_{NR}(\Omega_1,t_2,\Omega_3) \tag{21}$$

are obtained by adding the non-rephasing signal

$$\tilde{R}_{NR}(\Omega_1,t_2,\Omega_3) \equiv -\mathrm{Im}\left\{\int_0^{\infty} dt_1\int_0^{\infty} dt_3 e^{i\Omega_1 t_1} e^{i\Omega_3 t_3} R^{(5)}_{NR}(t_1,t_2,t_3)\right\} \tag{22}$$

and the rephasing signal

$$\tilde{R}_{R}(\Omega_1,t_2,\Omega_3) \equiv -\mathrm{Im}\left\{\int_0^{\infty} dt_1\int_0^{\infty} dt_3 e^{-i\Omega_1 t_1} e^{i\Omega_3 t_3} R^{(5)}_{R}(t_1,t_2,t_3)\right\} \tag{23}$$

transformed into the mixed time–frequency domain.

III. RESULTS AND DISCUSSION

We demonstrate the capacity of the presented calculation scheme to simulate R^5-2D line shapes of a strongly coupled molecular H-homodimer ($J > 0$) with average site energies $\bar{E}_1 = \bar{E}_2 \equiv \bar{E}$ and transition dipole moments $d_1 = d_2 \equiv d$. Similarly, the slow site energy fluctuations have the same fluctuation magnitudes σ_E and decorrelation timescale τ_E,

$$\Sigma^{(1)}_{11}(t) \equiv \Sigma^{(1)}_{22}(t) \equiv \sigma_E^2 e^{-t/\tau_E}, \tag{24}$$

but may have a variable degree of correlation $\beta \in [-1,1]$ between the two on-site fluctuations, i.e.,

$$\Sigma^{(1)}_{12}(t) \equiv \Sigma^{(1)}_{21}(t) \equiv \beta\sigma_E^2 e^{-t/\tau_E}. \tag{25}$$

The fluctuations of the bi-exciton binding energy

$$\Sigma^{(2)}(t) \equiv \sigma_\Delta^2 e^{-t/\tau_\Delta} \tag{26}$$

have magnitude σ_Δ and timescale τ_Δ and are chosen to be independent of single exciton fluctuations [$\Sigma^{(2-1)}(t) \equiv 0$]. We will often compare magnitudes of single exciton and bi-exciton fluctuations by the ratio

$$\gamma \equiv \frac{\sigma_\Delta}{\sigma_E}. \tag{27}$$

The optical line shapes are best analyzed in terms of transition frequencies,

$$\begin{aligned} \omega_{a_1 g}(t) &= \frac{E_1(t)+E_2(t)}{2} - \frac{1}{2}\sqrt{(E_1(t)-E_2(t))^2+4J^2}, \\ \omega_{a_2 g}(t) &= \frac{E_1(t)+E_2(t)}{2} + \frac{1}{2}\sqrt{(E_1(t)-E_2(t))^2+4J^2}, \\ \omega_{\alpha a_1}(t) &= \omega_{a_2 g}(t) + \Delta(t), \\ \omega_{\alpha a_2}(t) &= \omega_{a_1 g}(t) + \Delta(t), \\ \omega_{\alpha g}(t) &= E_1(t) + E_2(t) + \Delta(t), \end{aligned} \tag{28}$$

between instantaneous eigenstates (see Fig. 1) consisting of the collective ground state $|g\rangle$, the bi-exciton state

$$|\alpha\rangle = \hat{B}_1^\dagger \hat{B}_2^\dagger |g\rangle \tag{29}$$

and two delocalized single exciton states

$$\begin{aligned} |a_1(t)\rangle &= -\sin(\theta)\hat{B}_1^\dagger|g\rangle + \cos(\theta)\hat{B}_2^\dagger|g\rangle, \\ |a_2(t)\rangle &= \cos(\theta)\hat{B}_1^\dagger|g\rangle + \sin(\theta)\hat{B}_2^\dagger|g\rangle, \end{aligned} \tag{30}$$

with mixing angle

$$\theta(t) = \frac{1}{2}\mathrm{arccot}\left(\frac{E_1(t)-E_2(t)}{2J}\right). \tag{31}$$

Transition dipoles between excitonic states are given by

$$\begin{aligned} \mu_{a_1 g}(t) &= \mu_{\alpha a_1}(t) = d[\cos(\theta)-\sin(\theta)], \\ \mu_{a_2 g}(t) &= \mu_{\alpha a_2}(t) = d[\cos(\theta)+\sin(\theta)]. \end{aligned} \tag{32}$$

In the following simulations, we further simplified the transport dynamics and consider the gap between the single exciton

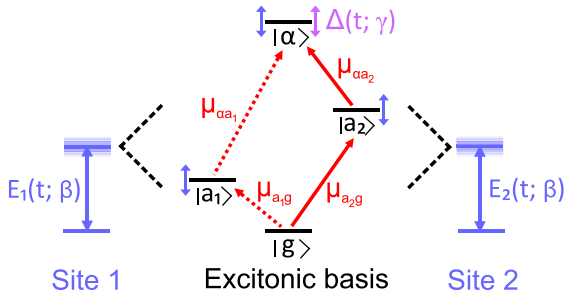

FIG. 1. Electronic energy level structure of the strongly coupled fluctuating dimer model discussed in the main text. The fluctuations inside the excitonic basis induced by site energies $E_n(t)$ and the bi-exciton binding energy $\Delta(t)$ are depicted with blue and violet arrows, respectively. The two dominant transitions of the homodimer are depicted with full red arrows, whereas transitions possible due to strong fluctuations (with respect to the coupling) are depicted with dashed arrows.

states to be much larger than the thermal energy so that the upward transport is negligible. Population dynamics are thus determined by two parameters: the rate constant k_R for population relaxation from the energetically higher lying single exciton state $|a_2\rangle$ to the lower lying single exciton state $|a_1\rangle$ and the rate k_A depleting population from bi-exciton state $|\alpha\rangle$.

In Secs. III A and III B, we compare R^5-2D line shapes of homodimers from which bi-exciton fluctuations are fully derived from on-site frequencies and have no autonomous spectral motions ($\gamma = 0$) with the case including additional autonomous bi-exciton fluctuations ($\gamma \neq 0$).

A. Non-autonomous bi-exciton fluctuations ($\gamma = 0$)

We start the discussion of the R^5-2D signals with a H-homodimer from which bi-exciton fluctuations are built up entirely from site energy fluctuations and have no independent (autonomous) component ($\gamma = 0$). The simulated R^5-2D line shapes in the slow annihilation limit ($k_A \ll k_R$) are depicted in Fig. 2 assuming uncorrelated [$\beta = 0$, (a)], correlated [$\beta = 1$, (b)], and anticorrelated [$\beta = -1$, (c)] on-site fluctuations.

We first recapitulate[12] the overall structure of the H-homodimer R^5-2D signal based on the inspection of double-sided Feynman diagrams depicted in Fig. 2(d): All diagrams evolve with coherence $|\alpha g\rangle\rangle$ during t_1 (i.e., with frequency $\omega_{\alpha g}$) corresponding to the observed peak positions at $\Omega_1 = 30\,000$ cm^{-1}. During t_3, the coherences oscillate with frequencies $\omega_{a_2 g} \approx 15\,800$ cm^{-1} [high-frequency negative peak, contributions are represented by the following pathways in Fig. 2(d): ground state bleach (GSB), single-quantum stimulated emission (1Q-SE), and EEA stimulated emission (EEA-SE)] and $\omega_{\alpha a_2} \approx 14\,200$ cm^{-1} [low-frequency positive peak, contributions are represented by the following pathways in Fig. 2(d): single-quantum excited state absorption (1Q-ESA), double-quantum stimulated emission (2Q-SE) and EEA excited state absorption (EEA-ESA)]. Their interference yields the observed two-peak structure at $t_2 = 0$ fs. The signal of the H-homodimer becomes dominated by the GSB diagram at long waiting times (panels of the second column from the left), and it reveals certain differences in the overall structure between the three panels when all transport and annihilation dynamics are finished ($k_R t_2 \gg 1$ and $k_A t_2 \gg 1$) and the lower, positive peak is damped. In the anticorrelated case, another negative low [magnified by 20% in Fig. 2(c)] frequency peak becomes apparent at $(\omega_{\alpha g}, \omega_{a_1 g})$. The feature appears due to the transient redistribution of the dipole moment strength toward the dark state[34] $|a_1\rangle$ as the fluctuations ($\sigma_E = 600$ cm^{-1}) are comparable to the excitonic coupling ($J = 800$ cm^{-1}). This effect also leads to the slightly asymmetric long time line shape of the uncorrelated case. Such a feature cannot be seen in the case of correlated fluctuations as the on-site energies are always identical, and no redistribution of the dipole moment strength is possible.

Having understood the overall peak structure, we next focus on the influence of dynamic disorder on the line shapes. To gain a deeper understanding of the relation between line shapes and disorder, we compare the line shapes [two leftmost panels of Figs. 2(a)–2(c)] with correlation statistics [two rightmost panels of Figs. 2(a)–2(c)] of the initial double (2Q) frequency $\omega_{\alpha g}(0)$ with delayed single (1Q) frequencies $\omega_{a_2 g}(t_2)$ relevant for the negative peak (blue points),

$$\tilde{P}_-(\Omega_1, t_2, \Omega_3) \equiv \langle \delta(\Omega_1 - \omega_{\alpha g}(0)) \delta(\Omega_3 - \omega_{a_2 g}(t_2)) \rangle, \tag{33}$$

and $\omega_{\alpha a_2}(t_2)$ relevant for the positive peak (orange points),

$$\tilde{P}_+(\Omega_1, t_2, \Omega_3) \equiv \langle \delta(\Omega_1 - \omega_{\alpha g}(0)) \delta(\Omega_3 - \omega_{\alpha a_2}(t_2)) \rangle, \tag{34}$$

obtained by diagonalizing 5000 sample trajectories [Eqs. (4) and (5)] of the Frenkel exciton Hamiltonian (1). Gaussian approximations to these 1Q-2Q statistics are given analytically in Appendix B for the general dimer model allowing for difference $E_\delta \equiv \tilde{E}_1 - \tilde{E}_2$ between site energies and general correlation matrix elements (3). The results of Appendix B are used in the main text in the homodimer limit: Eqs. (24) and (25) and $E_\delta = 0$ [except Eq. (39)].

The $t_2/\tau_E = 0$ R^5-2D maps of both the uncorrelated [Fig. 2(a)] and correlated [Fig. 2(b)] cases show that disorder induces elliptical and tilted line shapes. The magnitude of the tilt at zero delay time is quite similar for both peaks. After bath decorrelation at longer times ($t_2/\tau_E = 5$), the peak loses its tilt but remains elliptical.

The 1Q-2Q statistics of Figs. 2(a) and 2(b) resembles well the line shapes, differences between the two are largely ascribed to homogeneous broadening of the line shapes induced by the fast quantum coordinates. We can qualitatively understand the tilt's dynamics by calculating the principal axis of the elliptical contours [depicted in Figs. 2(a) and 2(b)] of the Gaussian approximation [see Eq. (B8) in Appendix B]. We find that the $t_2/\tau_E = 0$ line shapes and 1Q-2Q statistics are centered around lines,

$$\Omega_{3,\mp} = 0.5\Omega_1 \pm J, \tag{35}$$

as both single exciton $\omega_{a_2 g}(0) \propto \omega_{\alpha a_2}(0) \propto (E_1(0) + E_2(0))/2$ and bi-exciton $\omega_{\alpha g}(0) = E_1(0) + E_2(0)$ energies reflect the same combination of site energies. The general delay dependent angle between the principal and Ω_1 axis is given by

$$\tan(2\Phi_\pm(t_2)) = \frac{4}{3} C_E(t_2) \tag{36}$$

for both the positive (Φ_+) and negative (Φ_-) peaks with normalized correlation function

$$C_E(t) \equiv \frac{\Sigma_{11}^{(1)}(t)}{\Sigma_{11}^{(1)}(0)} = \frac{\Sigma_{22}^{(1)}(t)}{\Sigma_{22}^{(1)}(0)}. \tag{37}$$

The time dependence of the above tilts is a substantial difference to the GSB peak of R^3-2D, where $\tan(\Phi) = 1$ holds at all t_2 times.[18]

The case of anticorrelated sites ($\beta = -1$) depicted in Fig. 2(c) is vastly different compared to the above discussed cases: Both the negative and the positive peaks are not tilted and remain rather homogeneous. The reason is that the 2Q-energy $\omega_{\alpha g}(t) \equiv \omega_{\alpha g} \equiv 2\tilde{E}$ is stabilized by the anticorrelated motion of the sites for all waiting times and fluctuations of 1Q-energies are quadratic in $(E_1 - E_2)$ such that negligible inhomogeneous broadening occurs exclusively toward higher (lower) values of the mean frequencies of the negative (positive) peak along Ω_3.

Changing the type of on-site correlations affects the line shapes and the 1Q-2Q statistics (see Fig. 2). The latter is unfortunately not a direct spectroscopic observable, and the above characterization of dynamics by the principal axis (36) is limited to elliptic contours of Gaussian peaks. Next, we will thus inquire how the correlated spectral dynamics can be quantitatively extracted from the R^5-2D line shapes. To step beyond the limit of the elliptical line shapes, we adopt the concept of the center line[16–18] (CL) that quantifies the line shape

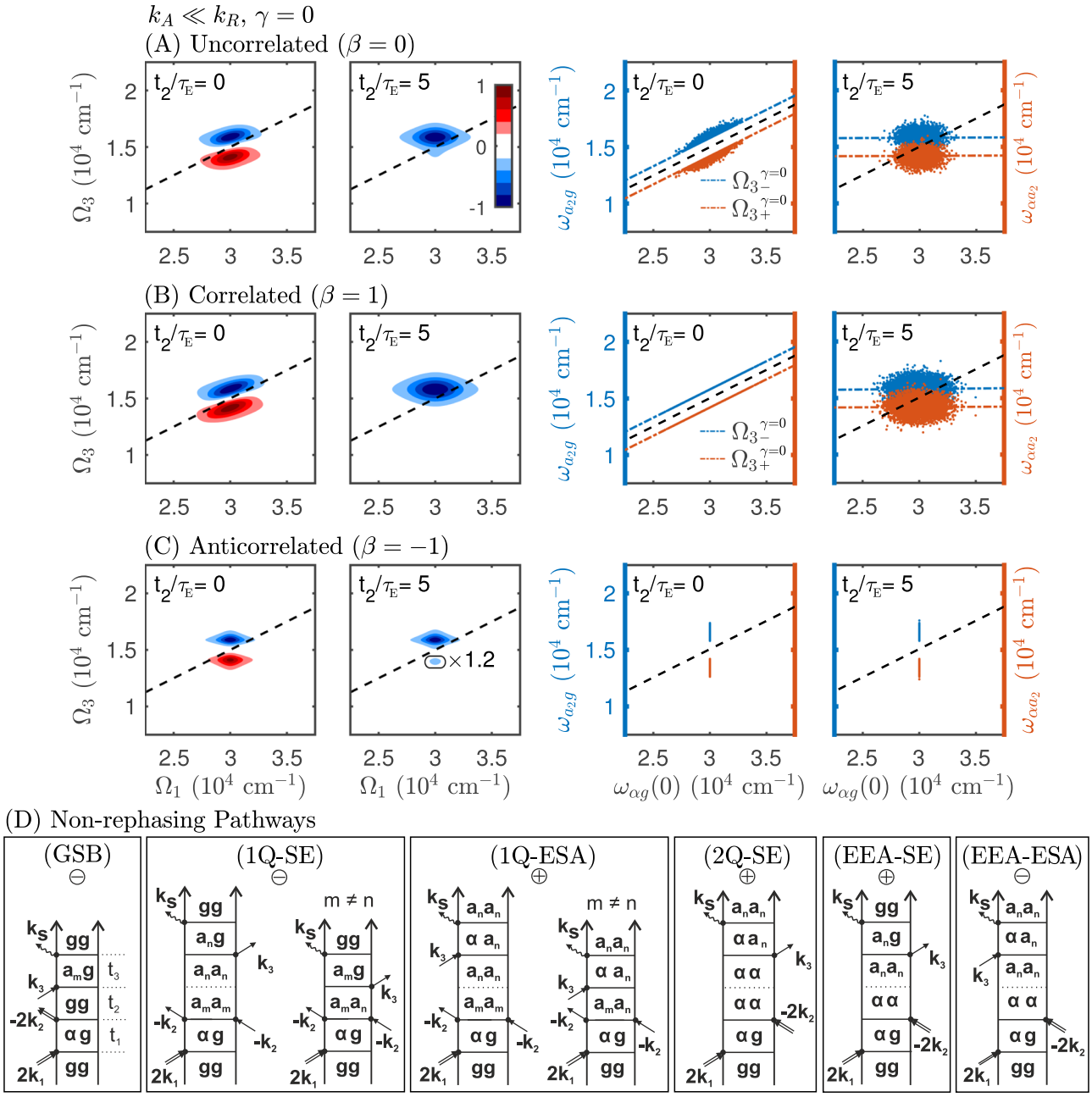

FIG. 2. The first two panels (from left to right) in (a)–(c) depict R^5-2D line shapes of a homodimer for two different waiting times assuming slow annihilation dynamics ($k_A \ll k_R$). We chose $\bar{E}$ = 15 000 cm^{-1}, J = 800 cm^{-1}, $\bar{\Delta}$ = 0 cm^{-1}, σ_E = 600 cm^{-1}, $\gamma = 0$, τ_E = 100 fs, k_A^{-1} = 100 fs, and k_R^{-1} = 30 fs, and all line shapes are averaged over 40 000 realizations of the OU process. Fluctuations on the two sites are assumed to be (top to bottom) uncorrelated, correlated, and anticorrelated. R^5-2D signals are normalized to their minimum value at each waiting time. The minor negative feature below the main peak in the $t_2/\tau_E = 5$ map of the anticorrelated case is magnified by 20%. The two panels on the right map the process of dynamic disorder by correlating frequencies $\omega_{\alpha a_2}(t_2)$ (orange) and $\omega_{a_2 g}(t_2)$ (blue) with frequency $\omega_{\alpha g}(0)$ obtained from the OU trajectories. The dashed black line depicts the line $\Omega_3 = 0.5\Omega_1$. (d) Non-rephasing double-sided Feynman diagrams contributing to the dimer signal. The rephasing pathways can be found in Ref. 12.

variability without any reference to a specific line shape type. The forward center line (FCL) [backward center line (BCL)] obtained by maximizing the signal along Ω_3 (Ω_1) for fixed Ω_1 (Ω_3) is depicted in Fig. 3(a). Their slopes around the peak center of the negative peak are further analyzed as a function of t_2 in Figs. 3(b) and 3(c) for the three correlation cases. The value of the FCL and inverse of the BCL slope at $t_2/\tau_E = 0$ shows a clear dependence on β as it is increased (decreased) with the amount of positive (negative) correlation with respect to the uncorrelated case as can be seen from Figs. 3(b) and 3(c).

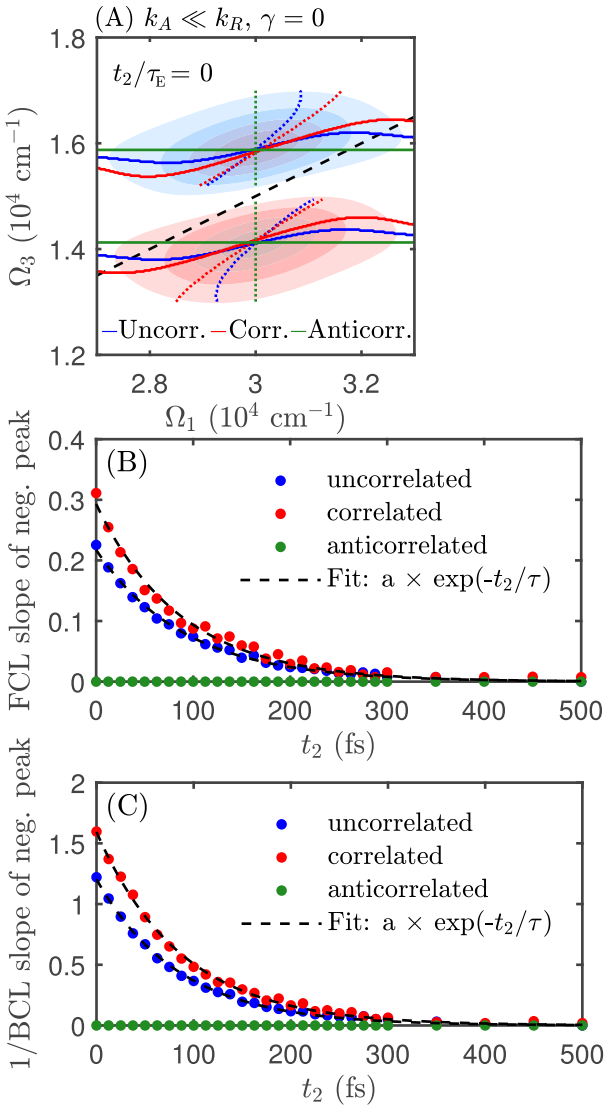

FIG. 3. (a) FCL (full lines) and BCL (dashed lines) for uncorrelated (blue), correlated (red), and anticorrelated (green) on-site fluctuations. The transparent R^5-2D line shapes in the background serve as a reference and are the same as in Fig. 2(a), i.e., uncorrelated and slow annihilation. (b) and (c) Slope of the FCL/BCL vs the waiting time t_2 for all correlation cases. The fit of the center line dynamics with a single exponential decay is depicted with dashed black lines.

The general temporal evolution of the negative peak's FCL and BCL slope is readily understood from analyzing the Gaussian approximation to the underlying statistics. We obtain

$$\left[\frac{\Omega_3 - \tilde{\omega}_{a_2 g}}{\Omega_1^{BCL} - \tilde{\omega}_{\alpha g}}\right]^{-1} = 2C_E(t_2), \qquad \frac{\Omega_3^{FCL} - \tilde{\omega}_{a_2 g}}{\Omega_1 - \tilde{\omega}_{\alpha g}} = \frac{1}{2}C_E(t_2), \tag{38}$$

for the time profile of the BCL and FCL, respectively. The evolution is thus governed by the correlation function $C_E(t_2)$, which describes an exponential decay with timescale τ_E. Fitting the FCL/BCL values obtained from the line shapes with a mono-exponential decay, we obtain a timescale of 90 fs ($\beta = 0$) or 85 fs ($\beta = 1$). Both values reflect well the relevant model input parameter, namely, the correlation timescale $\tau_E = 100$ fs. The center lines can thus be used to measure decorrelation similarly to R^3-2D.[18] Both the simulations depicted in Fig. 3 and the Gaussian analysis [symmetry Eq. (38)] additionally suggest that BCL and FCL report similarly on the tilts dynamics. However, in contrast to 2D-IR spectroscopy where a similar mirror symmetry is underlied by fundamental time reversal symmetry of stochastic dynamics at equilibrium [see Eq. (8) in Ref. 18], this observation here is approximate and limited to the present $\gamma = 0$ case (see Sec. III B).

While the Gaussian approximation to the CLs explains the observed decorrelation behavior, it is less successful to explain the sensitivity of the line shapes to inter-site correlation at zero, where vanishing sensitivity is predicted at $E_\delta = 0$, contrary to our simulations. The main problem with the analysis is that the approximate 1Q-2Q statistics does not capture the finite width of the distribution at $t_2/\tau_E = 0$ and more importantly has a singularity at that point in time. To remove the singularity, we investigate the 1Q-2Q statistics for finite but small site energy difference $E_\delta \neq 0$. The time profile of the FCL [Eq. (38)] is unchanged for the homodimer, but we obtain

$$\left[\frac{\Omega_3 - \tilde{\omega}_{a_2 g}}{\Omega_1^{BCL} - \tilde{\omega}_{\alpha g}}\right]^{-1} = \frac{2(1+\beta)}{1+\varepsilon^2+(1-\varepsilon^2)\beta}C_E(t_2), \tag{39}$$

with

$$\varepsilon = \frac{E_\delta}{\sqrt{E_\delta^2 + 4J^2}}, \tag{40}$$

for the BCL. The degree of on-site correlation β thus changes the BCL dynamics directly by changing the underlying 1Q-2Q statistics [see Eq. (39)], but the observed β-dependence of the FCL rests in an interference effect between the various homogeneous contributions as the width of the 1Q-2Q distribution is increased with increasing β [see Eq. (B11)]. One is tempted to conclude from this result that there is a degeneracy between the FCL of the correlated and a rescaled uncorrelated model with the same amount of homogeneous broadening; the general scaling factor between the models is $\sqrt{1+\beta}$. However, comparing the CLS-values from the correlated model ($\beta = 1$) to a rescaled uncorrelated model (scaling factor $\sqrt{2}$), we find appreciable differences between the two scenarios for the

negative R^5-2D peak. Specifically, there is a 3% difference between the FCLs and an 8% difference between the BCLs for the correlated and uncorrelated model. Hence, CLS analysis in R^5-2D gives access to the site energy correlations quantified by β. These results are appealing as they suggest that having experimental data at hand, one can only find agreement between experimental and theoretical FCL (BCL) slope dynamics if the correlation between the sites is taken into account, implying that the slope of the CLs can be used to parameterize the type and amount of inter-site correlation β and also the fluctuation timescales.

At long waiting times ($t_2/\tau_E \gg 1$), the line shapes are decorrelated (zero slope of FCL) and asymmetrically stretched, as the 2Q statistics seen along Ω_1 is broader than 1Q along Ω_3. The standard deviation along Ω_1 and Ω_3 for both negative and positive peaks satisfies the relation

$$\sigma^2_{\pm,\Omega_1} = 4\sigma^2_{\pm,\Omega_3}. \tag{41}$$

The anticorrelated line shapes remain homogeneous at all t_2 times as the 1Q-2Q statistics is stable.

The previous discussion of Figs. 2 and 3 was worked out for slow annihilation dynamics, which is not always the case in small molecular aggregates.[14,38] In the following, we check the sensitivity of the line shapes to inter-site correlations also for fast annihilation ($k_A^{-1} \gg k_R^{-1}$). This parameter setting modifies substantially the underlying homogeneous broadening of coherences $|\alpha g\rangle\rangle$ and $|\alpha a_2\rangle\rangle$, but not coherence $|a_2 g\rangle\rangle$. The negative peak is thus broadened along Ω_1 and the positive peak along Ω_1 and Ω_3 axis, as depicted in Figs. 4(a) and 4(b). The case of anticorrelated fluctuations is again special: A higher degree of localization and redistribution of dipole strength lifts the clear separation between GSB, 1Q-SE, 1Q-ESA, and 2Q-SE pathways. Additional pathways in coherence $|\alpha a_2\rangle\rangle$ or $|a_1 g\rangle\rangle$ in t_3 thus contribute to the positive peak. The interference between narrow/negative (GSB, 1Q-SE) and broad/positive (1Q-ESA, 2Q-SE) contributions along Ω_3 leads to a split peak that is positive at the edges and negative in its center. We reported similar features for weakly coupled homodimers and heterodimers in Ref. 12.

We will in the following focus on the FCL, which will be shown in Sec. III B to be sensitive to both parameters of interest, i.e., β and γ. The FCLs obtained from the simulations are depicted in Fig. 5. The slope values are generally decreased compared to the case of slow annihilation but have a similar β-dependence. The initial FCL value is thus a complex function of the degree and sign of the on-site correlation and also the model parameter defining the (in)homogeneous width.

B. Autonomous bi-exciton fluctuations ($\gamma \neq 0$)

Our conclusions so far were derived from a model that neglects bi-exciton binding energy fluctuations. This is a common assumption made to reduce the number of independent model parameters for the fluctuations of the second excitonic manifold. R^5-2D is, however, a promising candidate to indicate shortcomings of this assumption, as fluctuations of frequency $\omega_{\alpha g}$ are tracked vs the waiting time t_2. In this section, we will thus give the bi-exciton state more freedom to fluctuate, i.e., $\gamma \neq 0$; otherwise, the line shapes and

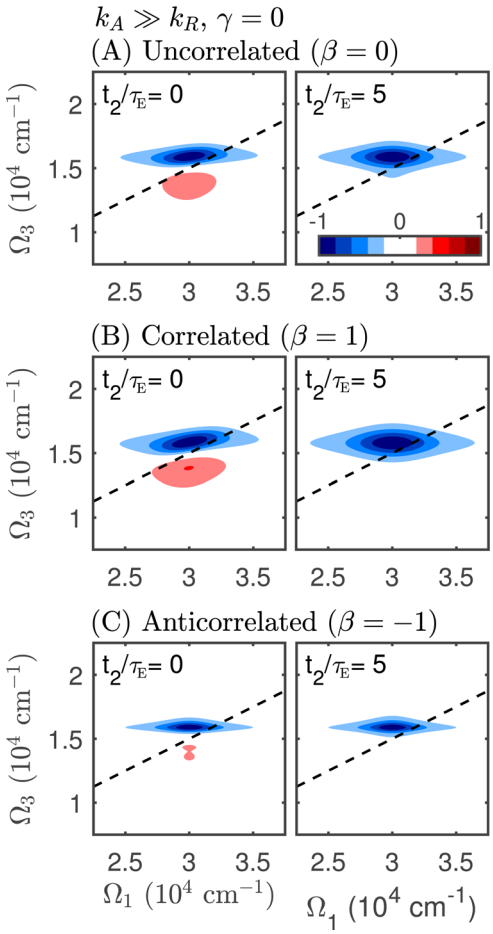

FIG. 4. R^5-2D line shapes of a homodimer assuming fast annihilation. We chose k_A^{-1} = 5 fs; other parameters are the same as in Fig. 2. The two sites are assumed to be (top to bottom) uncorrelated, correlated, and anticorrelated.

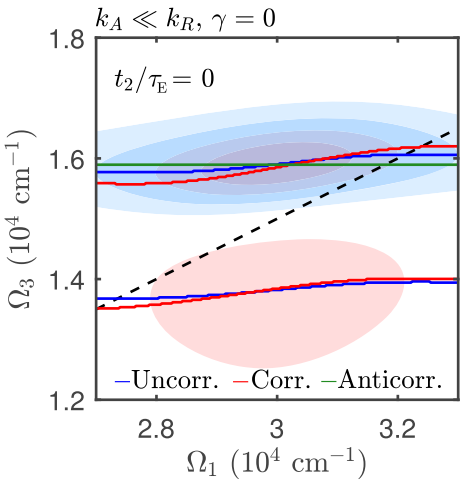

FIG. 5. FCL in the case of uncorrelated (blue), correlated (red), and anticorrelated (green) fluctuations. The transparent R^5-2D line shapes in the background are the same as in Fig. 4(a), i.e., uncorrelated fluctuations and fast annihilation.

1Q-2Q plots displayed in Fig. 6 are plotted for the same parameters as Fig. 2. Upon first inspection, we find that the tilts of the negative and positive peaks at $t_2/\tau_E = 0$ are quite different compared to the $\gamma = 0$ case for all values of β and still follow well the 1Q-2Q statistics plots shown on the right. To estimate the tilt, we again use the Gaussian approximation to the 1Q-2Q statistics and obtain

$$\begin{aligned}\tan[2\Phi_-(t_2)] &= \frac{2(1+\beta)}{\gamma^2+\frac{3}{2}(1+\beta)}C_E(t_2),\\ \tan[2\Phi_+(t_2)] &= \frac{\gamma^2 C_\Delta(t_2)+(1+\beta)C_E(t_2)}{\frac{3}{4}(1+\beta)},\end{aligned} \tag{42}$$

for the negative and positive peak, respectively, with the normalized correlation function of the bi-exciton fluctuations,

$$C_\Delta(t) \equiv \frac{\Sigma^{(2)}(t)}{\Sigma^{(2)}(0)}. \tag{43}$$

The timescale of the bi-exciton fluctuations τ_Δ is thus encoded in the evolution of the positive peak, which disappears for the H-homodimer. The lines $\Omega_{3,\pm}^{\beta,\gamma}$ are depicted in the 1Q-2Q plots of Figs. 6(a) and 6(b) for the respective β value and $\gamma = 2$ and follow well the tilt of the correlation plots. For uncorrelated fluctuations ($\beta = 0$) with the same decorrelation time profile [$C_E(t) = C_\Delta(t)$], we can directly relate γ to the ratio

$$\frac{\tan[2\Phi_+(t_2)]}{\tan[2\Phi_-(t_2)]} \approx \left(\frac{2}{3}\gamma^2+1\right)\left(\gamma^2+1\right) \tag{44}$$

of angles (42). The differences in slopes $\Phi_\pm(t_2)$ are, thus, a direct indication of finite γ.

The anticorrelated site energies are again special: The negative peak is inhomogeneously broadened along Ω_1 by σ_Δ and along Ω_3 by the quadratic site energy difference similar to the $\gamma = 0$ model. The positive peak displays a tilt as peaks are shifted along the lines,

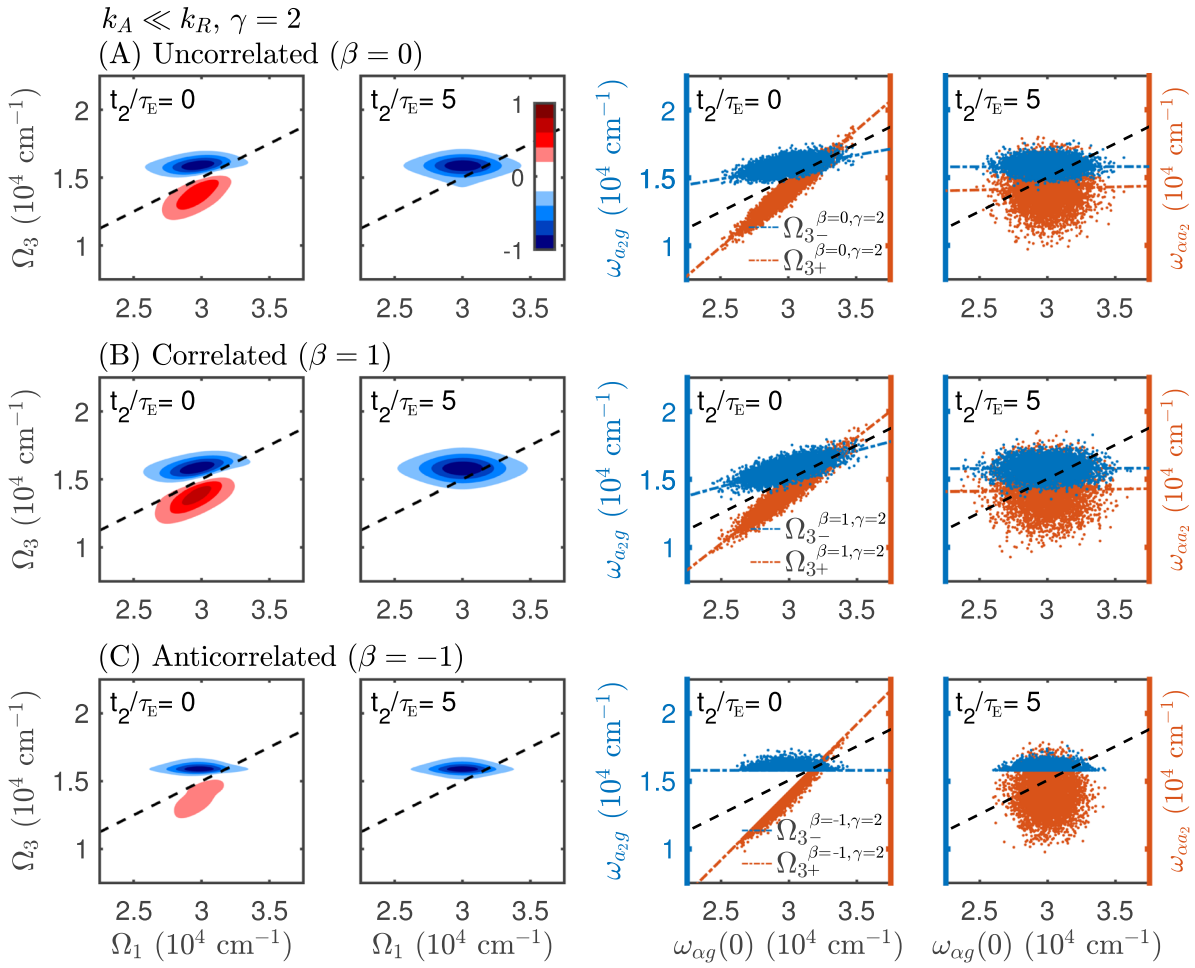

FIG. 6. Same as Figs. 2(a)–2(c), but $\gamma = 2$ and $\tau_E = \tau_\Delta = 100$ fs.

$$\Omega_{3,-}^{\beta=-1,\gamma\neq 0} = \tilde{E} + J,$$
$$\Omega_{3,+}^{\beta=-1,\gamma\neq 0} = \Omega_1 - \tilde{E} - J, \tag{45}$$

which leads to a slightly more homogeneous spectrum compared to the $\gamma = 0$ model.

The $t_2/\tau_E = 0$ line shapes depicted in Fig. 6 follow well their corresponding 1Q-2Q statistics, but the actual tilt (FCL/BCL slope) of the line shapes is again modified by model parameters defining homogeneous broadening. The degree of correlation β is again seen in the increasingly strict alignment of the negative peak's tilt, as depicted in Fig. 7. The positive peak shows a different behavior, as the FCL slope of the correlated case is smaller than the uncorrelated case, and the FCL slope of the anticorrelated case is not defined as the FCL displays a step due to the double-peak structure, similar to the discussed case of fast annihilation. The positive peak's slope of the H-homodimer should thus be analyzed carefully as it is not always well defined.

For the temporal evolution of the FCL and BCL of the negative peak, we find

$$\left[\frac{\Omega_3 - \tilde{\omega}_{a_2 g}}{\Omega_1^{BCL} - \tilde{\omega}_{\alpha g}}\right]^{-1} = 2C_E(t_2),$$
$$\frac{\Omega_3^{FCL} - \tilde{\omega}_{a_2 g}}{\Omega_1 - \tilde{\omega}_{\alpha g}} = \frac{1+\beta}{\gamma^2 + 2(1+\beta)} C_E(t_2), \tag{46}$$

highlighting the sensitivity of the FCL to both β and γ. The case of $\beta = -1$ is again special as the negative peak displays no line shape dynamics. The changes in the 1Q-2Q statistics of the positive peak are not visible in the line shapes as this peak disappears for the H-homodimer.

At long waiting times ($t_2/\tau_E \gg 1$), the line shapes are decorrelated [zero FCL, see Eq. (46)] and again asymmetrically stretched.

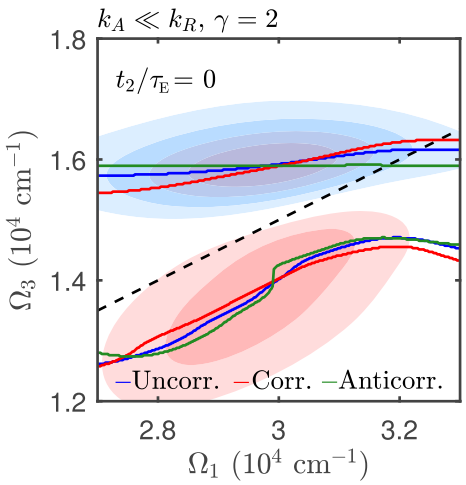

FIG. 7. FCL in the case of uncorrelated (blue), correlated (red), and anticorrelated (green) fluctuations. The transparent R^5-2D line shapes in the background are the same as in Fig. 6(a), i.e., uncorrelated and slow annihilation.

The standard deviations along Ω_1 and Ω_3 are, however, different for the negative

$$\sigma^2_{-,\Omega_1} \equiv 2(1+\beta)\sigma_E^2 + \sigma_\Delta^2,$$
$$\sigma^2_{-,\Omega_3} \equiv \frac{1}{2}(1+\beta)\sigma_E^2 \tag{47}$$

and positive

$$\sigma^2_{+,\Omega_1} = \sigma^2_{-,\Omega_1},$$
$$\sigma^2_{+,\Omega_3} \equiv \sigma^2_{-,\Omega_3} + \sigma_\Delta^2, \tag{48}$$

peak. From Eqs. (47) and (48), we can understand the observed additional stretching along Ω_1 as a result from the bi-exciton fluctuation magnitude σ_Δ^2.

IV. CONCLUSION

We present a model of spectral fluctuations in fifth-order spectroscopy of an excitonically coupled system and demonstrated that R^5-2D line shapes are able to quantify correlations between site energies, without the need to analyze beatings in R^3-2D signals. Hence, the methods discussed here can contribute to the discussion on the suggested role of site energy correlations in energy transport through biological light harvesting systems.[5,6]

In particular, we accounted for the effect of dynamic disorder in R^5-2D line shapes of a molecular H-homodimer. We based the model on the master equation formalism of Ref. 12, which ensures a thermodynamically consistent transport description and added a slow stochastic classical coordinate to address the peak tilt and its delay time dynamics. The timescale separation between the fast bath fluctuations responsible for transport and slow fluctuations inducing line-shaping effects is a key assumption for the present strategy and avoids the shortcomings of the individual components: purely homogeneous line shapes of a master equation approach and high temperature equilibrium between excitons set by stochastic quantum dynamics.[21] Justified alternatives to the present approach exist, but they are less feasible from a computational point of view: Stochastic quantum dynamics can be brought to finite temperatures by the hierarchical equations of motion (HEOM),[39] but procedures to calculate line shapes of multi-excitonic systems[34] or attempts to untangle HEOM into stochastic trajectories are numerically challenging even for the simplest aggregates.

In an extension of the strategy presented in Appendix B to approximate statistics of transition frequencies, the Gaussian character of typical noise can also justify a treatment of the diagonal fluctuations by the second cumulant,[33,37] while the effects of slow off-diagonal fluctuations on line shapes (beyond their contribution to transport rates) is omitted. Such an alternative strategy thus ignores, e.g., possible dipole redistribution, as discussed below Fig. 2(c) or in Ref. 34, and is not recommendable before more sophisticated accounts of off-diagonal disorder are included into the cumulant approach.[40]

Within our presented model, we found a tilt—quantified with the aid of CLS—of the R^5-2D line shapes and connected its waiting time dynamics with autocorrelation timescales of on-site fluctuations τ_E and bi-exciton binding energy fluctuations τ_Δ. We additionally found that the negative peak of the H-homodimer—related

TABLE I. Comparison of the correlation statistics of coherent 2D techniques (R^5-2D: $\pm 2\vec{K}_1 \mp 2\vec{K}_2 + \vec{K}_3$, R^3-2D: $\pm\vec{K}_1 \mp \vec{K}_2 + \vec{K}_3$, and 2Q-$R^3$-2D: $+\vec{K}_1 + \vec{K}_2 - \vec{K}_3$) measured on a homodimer. All signals display a two-peak structure reflecting transition frequencies ω_{ag} and $\omega_{\alpha a}$ along Ω_3, and both peaks are centered either at ω_{ag} or $\omega_{\alpha g}$ along Ω_1. Their line shapes, however, represent different types of correlation functions as summarized in this table.

Signal type	Correlation statistics related to the observed peaks
R^5-2D	$\langle\delta(\Omega_1 - \omega_{\alpha g}(0))\delta(\Omega_3 - \omega_{ag}(t_2))\rangle$
	$\langle\delta(\Omega_1 - \omega_{\alpha g}(0))\delta(\Omega_3 - \omega_{\alpha a}(t_2))\rangle$
R^3-2D	$\langle\delta(\Omega_1 - \omega_{ag}(0))\delta(\Omega_3 - \omega_{ag}(t_2))\rangle$
	$\langle\delta(\Omega_1 - \omega_{ag}(0))\delta(\Omega_3 - \omega_{\alpha a}(t_2))\rangle$
2Q-R^3-2D	$\langle\delta(\Omega_2 - \omega_{\alpha g}(0))\delta(\Omega_3 - \omega_{ag}(0))\rangle$
	$\langle\delta(\Omega_2 - \omega_{\alpha g}(0))\delta(\Omega_3 - \omega_{\alpha a}(0))\rangle$

to frequency pairs $(\omega_{\alpha g}(0), \omega_{a_2 g}(t_2))$—is generally better suited to extract CLS dynamics than the positive peak. A CLS analysis of the negative peak showed that the FCL of the peak is sensitive to both the amount of inter-site correlation β and the magnitude γ of independent bi-exciton binding energy fluctuations. As a rule of thumb, we find that the bi-exciton binding energies are fluctuating independently if the peaks of the H-dimer are asymmetrically tilted [see Eq. (44)] at $t_2/\tau_E = 0$.

Information about inter-site correlation is challenging to obtain from steady state[41–44] or third order time resolved spectroscopic techniques such as pump probe[45–47] or R^3-2D.[48,49] The main advantage of R^5-2D over these methods is that two-exciton fluctuations can be tracked over the waiting time period unlike linear and third-order techniques, as can be seen from Table I where we summarized the different correlation functions of various non-linear techniques to highlight this point.

These results shed new light on the R^5-2D technique as experimental and theoretical studies focused so far on the temporal evolution of specific peaks or the integrated signal to extract annihilation or diffusion timescales in molecular aggregates, but a line shape analysis—beyond pulse related artifacts[50]—has been omitted. We showed that R^5-2D line shapes are rich in information and are essential to analyze the coordination between spectral fluctuations of nearby molecules and bi-exciton binding energies.

ACKNOWLEDGMENTS

J.H. and C.H. acknowledge support by the Deutsche Forschungsgemeinschaft (DFG, German Research Foundation) through TUM International Graduate School of Science and Engineering (IGSSE), GSC 81, and funding by DFG under Germany's Excellence Strategy—EXC 2089/1-390776260. Mobility is supported by project "Exciton–exciton annihilation probed by non-linear spectroscopy" (MSMT Grant No. 8J19DE009, DAAD-Project No. 57444962).

AUTHOR DECLARATIONS

Conflict of Interest

The authors have no conflicts to disclose.

DATA AVAILABILITY

The data that support the findings of this study are available from the corresponding author upon reasonable request.

APPENDIX A: QUANTUM MASTER EQUATION FOR EXCITON TRANSPORT AND ANNIHILATION

In this appendix, we summarize for the reader's convenience the master equation model for exciton transport and annihilation. We follow closely our derivation presented in Ref. 12 for the stochastic version of the model in this work. We work in natural units where the Planck constant $\hbar$, the speed of light c, and the Boltzmann constant k_B are set to one, i.e., $\hbar = c = k_B = 1$.

We shall start with the time scale separation where the slow classical fluctuations are singled out from Eq. (1) and the free Hamiltonian[22]

$$\hat{H}_0(\{q\}) = \sum_{n=1}^{N} \hat{E}_n(\{q\})\hat{B}_n^\dagger \hat{B}_n + \sum_{\substack{n,m=1 \\ n\neq m}}^{N} J_{nm}\hat{B}_n^\dagger \hat{B}_m + \sum_{\substack{n,m=1 \\ n\neq m}}^{N} \frac{\hat{\Delta}_{nm}(\{q\})}{2}\hat{B}_n^\dagger \hat{B}_m^\dagger \hat{B}_n \hat{B}_m \tag{A1}$$

is considered at a fixed value of q. In contrast, the fast bath coordinates $\hat{Q}_n$ affecting the site energies are quantum and dynamical. Their time-dependent (Dirac) picture is defined with respect to the bath Hamiltonian, i.e., $\hat{Q}_n(t) \equiv e^{i\hat{H}_B t}\hat{Q}_n e^{-i\hat{H}_B t}$. We standardly assume $\hat{H}_B$ to be harmonic and, additionally, that coordinates $\hat{Q}_n$ are mutually uncorrelated and overdamped, i.e., the correlation function

$$C_n^{(Q)}(t) = \langle \hat{Q}_n(t)\hat{Q}_n \rangle \tag{A2}$$

assumes the form

$$\tilde{C}_n^{(Q)}(\omega) = \left[1 + \coth\left(\frac{\omega}{2T}\right)\right] 2\lambda_n \frac{\omega\Lambda_n}{\omega^2 + \Lambda_n^2} \tag{A3}$$

in the frequency domain ($\tilde{C}_n^{(Q)}(\omega) \equiv \int_{-\infty}^{\infty} C_n^{(Q)}(t)e^{-i\omega t}dt$).[51] The reorganization energy λ_n measures the magnitude of fluctuations, Λ_n is the bath relaxation rate ($\Lambda \gg \lambda$ defines the assumed fast bath limit), and T is the temperature.

The Redfield master equation (9) is a perturbative expansion in $\lambda \ll J$, and the dissipative (transport) dynamics thus appear between delocalized eigenstates $|\varepsilon_i(\{q\})\rangle$ of the Frenkel exciton Hamiltonian (A1) and the dissipative part of Eq. (10), thus, reads

$$\check{\mathscr{D}}(\{q\})|\rho(t)\rangle\rangle = \sum_{i,j=1;i\neq j}^{2^N} \Big[k_{\varepsilon_i\to\varepsilon_j}\Big(|\varepsilon_j\rangle\langle\varepsilon_i|\hat{\rho}(t)|\varepsilon_i\rangle\langle\varepsilon_j| - \frac{1}{2}\{|\varepsilon_i\rangle\langle\varepsilon_i|, \hat{\rho}(t)\}\Big) - \gamma^{pd}_{\varepsilon_i\varepsilon_j}|\varepsilon_i\rangle\langle\varepsilon_i|\hat{\rho}(t)|\varepsilon_j\rangle\langle\varepsilon_j| \Big], \tag{A4}$$

where $\{\hat{A}, \hat{B}\} \equiv \hat{A}\hat{B} + \hat{B}\hat{A}$. We omitted for readability the q dependence of the excitonic states, transport rates, and pure dephasing

rates on the right-hand side of Eq. (A4). Transport rates from the excitonic state $|\varepsilon_i(\{q\})\rangle$ to $|\varepsilon_j(\{q\})\rangle$ are given by

$$k_{\varepsilon_i\to\varepsilon_j}(\{q\}) = \sum_{n=1}^{N} \tilde{C}_n^{(Q)}(\omega_{\varepsilon_i\varepsilon_j})\left|\langle\varepsilon_i|\hat{B}_n^\dagger\hat{B}_n|\varepsilon_j\rangle\right|^2, \tag{A5}$$

where $\omega_{\varepsilon_i\varepsilon_j}(\{q\})$ is the electronic energy gap between eigenstates $|\varepsilon_i(\{q\})\rangle$ and $|\varepsilon_j(\{q\})\rangle$.

The pure dephasing rates $\gamma^{pd}_{\varepsilon_i\varepsilon_j}(\{q\})$ are given by

$$\gamma^{pd}_{\varepsilon_i\varepsilon_j}(\{q\}) = \frac{1}{2}\sum_{n=1}^{N}\tilde{C}_n^{(Q)}(0)\left[\langle\varepsilon_i|\hat{B}_n^\dagger\hat{B}_n|\varepsilon_i\rangle - \langle\varepsilon_j|\hat{B}_n^\dagger\hat{B}_n|\varepsilon_j\rangle\right]^2, \tag{A6}$$

where the limit $\omega \to 0$ of Eq. (A3) reads

$$\tilde{C}_n^{(Q)}(0) = \frac{4T\lambda_n}{\Lambda_n}. \tag{A7}$$

The fast bi-exciton bath coordinates $\hat{Q}_{nm}$ induce transport and fluctuations in complete analogy with Eqs. (A1)–(A7) (see Ref. 8). No bi-exciton transport is, however, possible for the presented dimer with a single bi-exciton state, and they thus solely induce trivial pure dephasing. The latter makes no appreciable difference to the line shapes and has thus been set to zero in the presented simulations of Figs. 2–7.

EEA is added to the model phenomenologically as unidirectional transport between excitonic manifolds differing in one quantum of excitation when adjacent chromophores are occupied,

$$\mathscr{A}|\rho(t)\rangle\rangle = \sum_{i=1}^{N-1} k_i^A\left(\left[\hat{L}_i^{(-)}\hat{\rho}\hat{L}_i^{(-)\dagger} - \frac{1}{2}\left\{\hat{L}_i^{(-)\dagger}\hat{L}_i^{(-)},\hat{\rho}(t)\right\}\right] + \left[\hat{L}_i^{(+)}\hat{\rho}\hat{L}_i^{(+)\dagger} - \frac{1}{2}\left\{\hat{L}_i^{(+)\dagger}\hat{L}_i^{(+)},\hat{\rho}(t)\right\}\right]\right). \tag{A8}$$

The operators

$$\hat{L}_i^{(-)} \equiv B_{i+1}^\dagger B_{i+1} B_i \tag{A9}$$

and

$$\hat{L}_i^{(+)} \equiv B_i^\dagger B_i B_{i+1} \tag{A10}$$

describe, respectively, EEA with rate k_i^A at site i ($\hat{L}_i^{(-)}$) or $i+1$ ($\hat{L}_i^{(+)}$), if two excitons are present at sites i and $i+1$.

APPENDIX B: GAUSSIAN APPROXIMATION TO 1Q-2Q STATISTICS

The 1Q-2Q statistics defined in Eqs. (33) and (34) can be approximated by a bivariate Gaussian distribution for small fluctuations. To obtain analytical expressions, we expand eigenenergies (28) linearly in stochastic coordinates $\{q(t)\}$,

$$\begin{aligned}
\omega_{\alpha g}(t) &= \bar{\omega}_{\alpha g} + \delta E_1(t) + \delta E_2(t) + \delta\Delta(t),\\
\omega_{a_2 g}(t) &\approx \bar{\omega}_{a_2 g} + \frac{\delta E_1(t)+\delta E_2(t)}{2} + \frac{E_\delta}{2}\frac{\delta E_1(t)-\delta E_2(t)}{\sqrt{E_\delta^2+4J^2}},\\
\omega_{\alpha a_2}(t) &= \omega_{\alpha g}(t) - \omega_{a_2 g}(t)\\
&\approx \bar{\omega}_{\alpha a_2} + \frac{\delta E_1(t)+\delta E_2(t)}{2}\\
&\quad - \frac{E_\delta}{2}\frac{\delta E_1(t)-\delta E_2(t)}{\sqrt{E_\delta^2+4J^2}} + \delta\Delta(t).
\end{aligned} \tag{B1}$$

We allow for the general dimer model with small site energy difference

$$E_\delta \equiv \bar{E}_1 - \bar{E}_2, \tag{B2}$$

with fluctuation profiles

$$\begin{aligned}
\delta E_{1,2}(t) &= E_{1,2}(t) - \bar{E}_{1,2},\\
\delta\Delta(t) &= \Delta(t) - \bar{\Delta},
\end{aligned} \tag{B3}$$

and mean transition energies

$$\begin{aligned}
\bar{\omega}_{\alpha g} &\equiv \bar{E}_1 + \bar{E}_2 + \bar{\Delta},\\
\bar{\omega}_{a_2 g} &\equiv \frac{\bar{E}_1+\bar{E}_2}{2} + \sqrt{\left(\frac{E_\delta}{2}\right)^2 + J^2},\\
\bar{\omega}_{\alpha a_2} &\equiv \frac{\bar{E}_1+\bar{E}_2}{2} - \sqrt{\left(\frac{E_\delta}{2}\right)^2 + J^2} + \bar{\Delta}.
\end{aligned} \tag{B4}$$

This general dimer model with small site energy difference E_δ provides insight into certain line shape singularities treated in Eq. (39).

As the Gaussian character of the distributions is maintained under linear transformations (B1), we finally arrive at the following bivariate Gaussian distributions for the 1Q-2Q statistics:

$$\begin{aligned}
&\tilde{P}_\pm(\Omega_{1,\pm}, t_2, \Omega_{3,\pm})\\
&\quad\approx \frac{1}{2\pi b_\pm(t_2)}(\exp) - \frac{\Omega_{1,\pm}^2\sigma_{\pm,\Omega_3}^2 + \Omega_{3,\pm}^2\sigma_{\pm,\Omega_1}^2 - 2\Omega_{1,\pm}\Omega_{3,\pm}\xi_\pm(t_2)}{2b_\pm^2(t_2)},
\end{aligned} \tag{B5}$$

with the definitions for the negative

$$
\begin{aligned}
\Omega_{1,-} &\equiv \Omega_1 - \tilde{\omega}_{\alpha g},\\
\Omega_{3,-} &\equiv \Omega_3 - \tilde{\omega}_{a_2 g},\\
\sigma^2_{-,\Omega_1} &\equiv \Sigma^{(2)}(0) + \Sigma^{(1)}_{11}(0) + 2\Sigma^{(1)}_{12}(0) + \Sigma^{(1)}_{22}(0),\\
\sigma^2_{-,\Omega_3} &\equiv \frac{1}{4}\left(\left[1+\frac{E_\delta}{\sqrt{E_\delta^2+4J^2}}\right]^2\Sigma^{(1)}_{11}(0)+2\Sigma^{(1)}_{12}(0)\left(1-\frac{E_\delta^2}{E_\delta^2+4J^2}\right)\right.\\
&\quad\left.+\left[1-\frac{E_\delta}{\sqrt{E_\delta^2+4J^2}}\right]^2\Sigma^{(1)}_{22}(0)\right),\\
\xi_-(t_2) &\equiv \frac{1}{2}\left(\left[1+\frac{E_\delta}{\sqrt{E_\delta^2+4J^2}}\right]\Sigma^{(1)}_{11}(t_2)+2\Sigma^{(1)}_{12}(t_2)\right.\\
&\quad\left.+\left[1-\frac{E_\delta}{\sqrt{E_\delta^2+4J^2}}\right]\Sigma^{(1)}_{22}(t_2)\right),\\
b^2_-(t_2) &\equiv \sigma^2_{-,\Omega_1}\sigma^2_{-,\Omega_3} - \xi^2_-(t_2)
\end{aligned}
\tag{B6}
$$

and positive

$$
\begin{aligned}
\Omega_{1,+} &\equiv \Omega_1 - \tilde{\omega}_{\alpha g},\\
\Omega_{3,+} &\equiv \Omega_3 - \tilde{\omega}_{\alpha a_2},\\
\sigma^2_{+,\Omega_1} &= \sigma^2_{-,\Omega_1},\\
\sigma^2_{+,\Omega_3} &\equiv \frac{1}{4}\left(\left[1-\frac{E_\delta}{\sqrt{E_\delta^2+4J^2}}\right]^2\Sigma^{(1)}_{11}(0)+2\Sigma^{(1)}_{12}(0)\left(1-\frac{E_\delta^2}{E_\delta^2+4J^2}\right)\right.\\
&\quad\left.+\left[1+\frac{E_\delta}{\sqrt{E_\delta^2+4J^2}}\right]^2\Sigma^{(1)}_{22}(0)\right)+\Sigma^{(2)}(0),\\
\xi_+(t_2) &\equiv \frac{1}{2}\left(\left[1-\frac{E_\delta}{\sqrt{E_\delta^2+4J^2}}\right]\Sigma^{(1)}_{11}(t_2)+2\Sigma^{(1)}_{12}(t_2)\right.\\
&\quad\left.+\left[1+\frac{E_\delta}{\sqrt{E_\delta^2+4J^2}}\right]\Sigma^{(1)}_{22}(t_2)\right)+\Sigma^{(2)}(t_2),\\
b^2_+(t_2) &\equiv \sigma^2_{+,\Omega_1}\sigma^2_{+,\Omega_3} - \xi^2_+(t_2)
\end{aligned}
\tag{B7}
$$

2D peaks. Equation (B5) can be formally identified with the absorptive line shapes if the slow ($\sigma\tau \gg 1$) diagonal spectral fluctuations are the only relevant dynamical process, i.e., when transport and annihilation dynamics are neglected. The time-dependent angle of the principal axis of elliptic contours (B5) reads

$$
\tan[2\Phi_\pm(t_2)] = \frac{2\xi_\pm(t_2)}{\sigma^2_{\pm,\Omega_1} - \sigma^2_{\pm,\Omega_3}}. \tag{B8}
$$

The FCL and BCL of the positive and negative peak are obtained with

$$
\begin{aligned}
\frac{\partial}{\partial\Omega_1}\tilde{P}_\pm(\Omega_1,t_2,\Omega_3)\Big|_{\Omega_1=\Omega_1^{BCL}} &= 0,\\
\frac{\partial}{\partial\Omega_3}\tilde{P}_\pm(\Omega_1,t_2,\Omega_3)\Big|_{\Omega_3=\Omega_3^{FCL}} &= 0,
\end{aligned}
\tag{B9}
$$

and read

$$
\begin{aligned}
\left[\frac{\Omega_{3,\pm}}{\Omega^{BCL}_{1,\pm}}\right]^{-1} &= \frac{\xi_\pm(t_2)}{\sigma^2_{\pm,\Omega_3}},\\
\left[\frac{\Omega^{FCL}_{3,\pm}}{\Omega_{1,\pm}}\right] &= \frac{\xi_\pm(t_2)}{\sigma^2_{\pm,\Omega_1}}.
\end{aligned}
\tag{B10}
$$

The diagonal (major) and anti-diagonal (minor) semidiameter of elliptical contours (B5) are given by

$$
\begin{aligned}
\sigma^2_{\text{diag},\pm} &= \frac{\sigma^2_{\pm,\Omega_1}+\sigma^2_{\pm,\Omega_3}}{2} + \sqrt{\left(\frac{\sigma^2_{\pm,\Omega_1}-\sigma^2_{\pm,\Omega_3}}{2}\right)^2+\xi^2_\pm(t_2)},\\
\sigma^2_{anti-\text{diag},\pm} &= \frac{\sigma^2_{\pm,\Omega_1}+\sigma^2_{\pm,\Omega_3}}{2} - \sqrt{\left(\frac{\sigma^2_{\pm,\Omega_1}-\sigma^2_{\pm,\Omega_3}}{2}\right)^2+\xi^2_\pm(t_2)},
\end{aligned}
\tag{B11}
$$

respectively.

The limit of $E_\delta = 0$ is used to derive Eqs. (35), (36), (38), (41), (42), and (46)–(48) of the main text. The full $\tilde{E}_\delta \neq 0$ form is helpful to approach the line shape singularity for $\gamma = 0$ at $t_2 = 0$ fs [see Eq. (39)].

REFERENCES

[1] T. Renger, V. May, and O. Kühn, Phys. Rep. **343**, 137 (2001).
[2] S. F. Huelga and M. B. Plenio, Contemp. Phys. **54**, 181 (2013).
[3] V. Perlík, J. Seibt, L. J. Cranston, R. J. Cogdell, C. N. Lincoln, J. Savolainen, F. Šanda, T. Mančal, and J. Hauer, J. Chem. Phys. **142**, 212434 (2015).
[4] J. C. Dean, T. Mirkovic, Z. S. D. Toa, D. G. Oblinsky, and G. D. Scholes, Chem **1**, 858 (2016).
[5] B. S. Rolczynski, H. Zheng, V. P. Singh, P. Navotnaya, A. R. Ginzburg, J. R. Caram, K. Ashraf, A. T. Gardiner, S.-H. Yeh, S. Kais, R. J. Cogdell, and G. S. Engel, Chem **4**, 138 (2018).
[6] J. Cao, R. J. Cogdell, D. F. Coker, H.-G. Duan, J. Hauer, U. Kleinekathöfer, T. L. C. Jansen, T. Mančal, R. J. D. Miller, J. P. Ogilvie, V. I. Prokhorenko, T. Renger, H.-S. Tan, R. Tempelaar, M. Thorwart, E. Thyrhaug, S. Westenhoff, and D. Zigmantas, Sci. Adv. **6**, eaaz4888 (2020).
[7] L. Wang, M. A. Allodi, and G. S. Engel, Nat. Rev. Chem. **3**, 477 (2019).
[8] O. Rancova, R. Jankowiak, and D. Abramavicius, J. Phys. Chem. B **122**, 1348 (2018).
[9] B. Brüggemann and T. Pullerits, New J. Phys. **13**, 025024 (2011).
[10] J. Dostál, F. Fennel, F. Koch, S. Herbst, F. Würthner, and T. Brixner, Nat. Commun. **9**, 2466 (2018).
[11] V. May, J. Chem. Phys. **140**, 054103 (2014).
[12] C. Heshmatpour, J. Hauer, and F. Šanda, Chem. Phys. **528**, 110433 (2020).
[13] J. Lüttig, T. Brixner, and P. Malý, J. Chem. Phys. **154**, 154202 (2021).
[14] C. Heshmatpour, P. Malevich, F. Plasser, M. Menger, C. Lambert, F. Šanda, and J. Hauer, J. Phys. Chem. Lett. **11**, 7776 (2020).
[15] P. Malý, J. Lüttig, A. Turkin, J. Dostál, C. Lambert, and T. Brixner, Chem. Sci. **11**, 456 (2020).
[16] S. T. Roberts, J. J. Loparo, and A. Tokmakoff, J. Chem. Phys. **125**, 084502 (2006).
[17] K. Kwak, S. Park, I. J. Finkelstein, and M. D. Fayer, J. Chem. Phys. **127**, 124503 (2007).

[18]F. Šanda, V. Perlík, C. N. Lincoln, and J. Hauer, J. Phys. Chem. A **119**, 10893 (2015).
[19]F. Šanda and S. Mukamel, Phys. Rev. Lett. **98**, 080603 (2007).
[20]G. E. Uhlenbeck and L. S. Ornstein, Phys. Rev. **36**, 823 (1930).
[21]R. Kubo, J. Phys. Soc. Jpn. **9**, 935 (1954).
[22]J. Frenkel, Phys. Rev **37**, 1276 (1931).
[23]V. Sláma, V. Perlík, H. Langhals, A. Walter, T. Mančal, J. Hauer, and F. Šanda, Front. Chem. **8**, 579166 (2020).
[24]D. Abramavicius, B. Palmieri, D. V. Voronine, F. Šanda, and S. Mukamel, Chem. Rev. **109**, 2350 (2009).
[25]M. D. Donsker, Mem. Am. Math. Soc. **6**, 1 (1951).
[26]N. J. Higham, Wiley Interdiscip. Rev.: Comput. Stat. **1**, 251 (2009).
[27]V. May and O. Kuhn, *Charge and Energy Transfer Dynamics in Molecular Systems* (Wiley-VCH Verlag, 2011).
[28]A. G. Redfield, IBM J. Res. Dev. **1**, 19 (1957).
[29]T. Pullerits, M. Chachisvilis, and V. Sundström, J. Phys. Chem. **100**, 10787 (1996).
[30]B. Brüggemann, J. L. Herek, V. Sundström, T. Pullerits, and V. May, J. Phys. Chem. B **105**, 11391 (2001).
[31]B. Brüggemann, N. Christensson, and T. Pullerits, Chem. Phys. **357**, 140 (2009).
[32]R. Kubo, J. Phys. Soc. Jpn. **12**, 570 (1957).
[33]S. Mukamel, *Principles of Nonlinear Optical Spectroscopy* (Oxford University Press, 1995).
[34]F. Šanda and S. Mukamel, J. Phys. Chem. B **112**, 14212 (2008).
[35]U. Fano, Rev. Mod. Phys. **29**, 74 (1957).
[36]R. W. Zwanzig, *Lectures in Theoretical Physics* (Interscience, New York, NY, 1960), Vol. 3, p. 106.
[37]V. Perlík and F. Šanda, J. Chem. Phys. **147**, 084104 (2017).
[38]P. Malý, S. Mueller, J. Lüttig, C. Lambert, and T. Brixner, J. Chem. Phys. **153**, 144204 (2020).
[39]Y. Tanimura, J. Chem. Phys. **153**, 020901 (2020).
[40]D. Abramavicius, L. Valkunas, and S. Mukamel, Europhys. Lett. **80**, 17005 (2007).
[41]F. Domínguez-Adame, Phys. Rev. B **51**, 12801 (1995).
[42]V. A. Malyshev, A. Rodríguez, and F. Domínguez-Adame, Phys. Rev. B **60**, 14140 (1999).
[43]E. W. Knapp, Chem. Phys. **85**, 73 (1984).
[44]M. Bednarz and P. Reineker, J. Lumin. **119–120**, 482 (2006).
[45]J. Knoester, J. Lumin. **58**, 107 (1994).
[46]J. Knoester, J. Chem. Phys. **99**, 8466 (1993).
[47]J. R. Durrant, J. Knoester, and D. A. Wiersma, Chem. Phys. Lett. **222**, 450 (1994).
[48]D. Abramavicius and S. Mukamel, J. Chem. Phys. **134**, 174504 (2011).
[49]J. Lim, D. J. Ing, J. Rosskopf, J. Jeske, J. H. Cole, S. F. Huelga, and M. B. Plenio, J. Chem. Phys. **146**, 024109 (2017).
[50]T. N. Do, L. Chen, A. K. Belyaev, H.-S. Tan, and M. F. Gelin, Chem. Phys. **515**, 119 (2018).
[51]A. O. Caldeira and A. J. Leggett, Physica A **121**, 587 (1983).